Unconventional Photo-Control of Structural Features Using Elliptically Polarized Light

Srinivas Pagidi, Sujaya Kumar Vishwanath, Dan Luo, Surajit Dhara, and Ramesh Manda*

The holographic interference of either same-handed or orthogonal polarized beams is commonly employed in the fabrication of optical elements as it enables the development of an ideal sinusoidal surface modulation by inducing the mass migration of photochromic polymer. However, this approach encounters challenges in producing multiplexed optical elements with a complex surface topography, primarily due to only sinusoidal surface topography which limits control over the feature's shape and size. Here, a versatile approach is demonstrated for fabricating spatially multiplexed optical elements using ellipticity-controlled orthogonally elliptically polarized (OEP) beams that offer distorted square-like and rhombus-like pillars on the azopolymer layer by asymmetric azopolymer migration driven by spatially varying ellipticity and azimuth angle of interference beam. These multiplexed distorted shapes enable selective energy transfer during light diffraction and also induce a $\pi/8$ phase-shift to polarization states. Ellipticity control of both writing and interference beams provides an additional degree of freedom for structuring the surface topography of optical elements. Furthermore, a quantitative analysis of the multiplexed OEP surface relief is performed to achieve distinct diffraction properties, thereby rendering its suitability for fabricating complex optical elements.

1. Introduction

The Holography or Holographic Interferometry (HI) technique is a versatile one-step fabrication process to produce large-scale sinusoidal surface modulations for engineering optical elements. For instance, head-mounted 3D display devices, such as augmented reality (AR) and virtual reality (VR), consist of various optical elements with specific structures designed to direct the display beam into viewer's eye.[1–4] These optical elements having precisely engineered structures are used to guide the light in the desired direction. Despite the recent development of various techniques for structuring the topography of optical elements, the two-beam HI technique remains the most efficient due to several advantages, including seamless inscription, low cost, single writing, and sinusoidal topography.[5–10] This technique enables the encoding of amplitude, phase, and polarization information. Furthermore, the demand for HI is highlighted by the emergence of the holographic display, photonic crystal (PC), and optical Fourier elements (OFE).[11–16]

The two-beam HI technique involves the intensity interference pattern (IIP), driven by gradient force generated by polarized beams of the same-handedness, and the polarization interference pattern (PIP), relying on spatially varying polarization created by orthogonally polarized beams for surface modulation.[17–20] Both interference patterns are generally inscribed onto photochromic materials capable of reversible spontaneous photoisomerization between *trans-* and *cis-*isomers, initiating the spatial migration of azopolymer. Specifically, the inherent tendency of azobenzene molecules to align perpendicular to the electric field vector of the polarized beam (called orientational hole burning) facilitates mass migration of azopolymer in PIP. Conversely, in IIP, the gradient force exerted on the azobenzene material in a direction parallel to the grating vector drags the bulk azopolymer chain and creates spatial modulation of permittivity. The azobenzene in high-intensity areas is anticipated to move toward the dark area in IIP. In PIP, azobenzene in regions where the polarization axis is parallel to the grating axis moves toward areas where the polarization axis is perpendicular.[21–26] Both IIP and PIP differ in the azopolymer migration mechanism and exhibit differences in diffraction properties, such as modulation height and diffraction efficiency (DE). For example, the PIP approach stores polarization information so that the polarization state of the diffracted beam depends on the readout beam, which could be advantageous with compared to IIP. Various optical elements such as volume holographic gratings, polarization gratings, and Pancharatnam–Berry phase lenses for AR, VR, and mixed reality (MR) have been demonstrated by using this

S. Pagidi, D. Luo
Department of Electrical and Electronic Engineering
Southern University of Science and Technology
Xueyuan Road 1088, Nanshan District, Shenzhen, Guangdong 518055, China
S. K. Vishwanath
Center for Nano Science and Engineering
Indian Institute of Science
Bangalore, Karnataka 560012, India
S. Dhara, R. Manda
School of Physics
University of Hyderabad
Gachibowli, Hyderabad, Telangana 500046, India
E-mail: manda_rff@uohyd.ac.in

technique.[27–31] However, this approach relies on the polarization state of the interfering beams being either linearly polarised (LP) or circularly polarized (CP), thus restricting the degree of freedom in designing a surface topography. For instance, the fabrication of PC and OFE necessitates generating complex structures and subsequent reconstruction to produce 3D depth cues.[12,14,32] Clearly, a non-trivial approach allowing a high degree of freedom to design the surface profile and enabling non-sinusoidal surface modulation is highly desirable.

The recent development of orthogonal elliptically polarized (OEP) holography, which enables asymmetric control of azopolymer migration, is considered a vital technique for overcoming the aforementioned challenges.[33–35] The control over the writing elliptically polarized (EP) beam enables the formation of more complex and finely tuned surface-modulated structures, resulting in high-performing holographic optical elements. This technique also offers the advantage of eliminating the need for the polarization of the read-out beam to match the writing beam. Consequently, this increases the flexibility in achieving accurate and faithful as well as null reconstruction.[36–39] However, the underlying mechanism of azopolymer migration and the impact of ellipticity remain unclear. Hence, further studies employing OEP technique, which enables precise control over the surface modulation and desired diffraction, is the need of the hour.

In this paper, we propose an unconventional approach for fabricating spatially multiplexed optical elements utilizing ellipticity-modulated OEP beams. Our approach enables asymmetric control of 3D surface modulation and introduces an additional dimension of control over the shape and size of structural features. Moreover, ellipticity-modulated OEP beams facilitates the creation of square and rhombus-shaped pillars, leading to asymmetric spatial modulation of diffracted light and polarization states.

2. Theory

The superposition of two orthogonal polarized beams generates a spatial distribution of polarized states, arising from the vector sum of their respective electric field vectors. This vectorial interference can be represented by the Jones vector, a two-element complex vector consisting of the amplitude and phase of the electric field vectors in orthogonal directions. This formalism simplifies the analysis and manipulation of polarized light as it interacts with optical elements. The addition of Jones vectors describes the spatial distribution of the resultant vector based on the combination of polarizations. In Jones vector formalism, left-handed circularly polarized (LCP) light is represented as, $E_{LCP} = \frac{1}{\sqrt{2}} \begin{bmatrix} 1 \\ i \end{bmatrix} e^{i\varphi_1}$, and the right-handed circularly polarization (RCP) light as, $E_{RCP} = \frac{1}{\sqrt{2}} \begin{bmatrix} 1 \\ -i \end{bmatrix} e^{i\varphi_2}$, where φ_1 and φ_2 are the initial phases of LCP and RCP, respectively. A schematic representation of E_{RCP} is shown in **Figure 1a**. Both LCP and RCP are orthogonal (i.e., $E_{LCP} \cdot E_{RCP}^\dagger = E_{LCP}^\dagger \cdot E_{RCP} = 0$), and the resultant polarization vector ($E_{LCP-RCP}$) of interference can be expressed as:[40]

$$E_{LCP-RCP} = \sqrt{2} \begin{bmatrix} \cos \delta \\ \sin \delta \end{bmatrix} \tag{1}$$

where δ ($= \varphi_2 - \varphi_1 = \frac{2\pi x}{\Lambda}$) is the phase difference between the two writing beams, dependent on spatial positions (x) and pitch (Λ). The resultant vector $E_{LCP-RCP}$ depicts the in-plane spatial distribution of LP along the grating axis ($k_G = \frac{2\pi}{\Lambda}$) as a function of δ, as illustrated in Figure 1b. This spatially distributed LP guides the directional mass migration of the photo-isometric polymer along the k_G. The k_G represents the direction perpendicular to the periodic surface grooves on the photo-isomeric material, which determines the orientation of the diffraction pattern.

Similarly, the Jones vector representation for EP with specific azimuth (θ) and ellipticity (e) can be expressed as:[41]

$$E_{LEP} = \frac{1}{\sqrt{a^2 + b^2 + c^2}} \begin{bmatrix} a \\ b + ic \end{bmatrix} e^{i\varphi_1} \tag{2}$$

$$E_{REP} = \frac{1}{\sqrt{a^2 + b^2 + c^2}} \begin{bmatrix} a - ic \\ -b \end{bmatrix} e^{i\varphi_2} \tag{3}$$

where a and b are the semi-major and semi-minor axes of the ellipse, respectively, and c is the imaginary part of the amplitude when the EP is inclined. Figure 1a illustrates E_{REP} (Equation (3)), showing E_{REP} vector reaches its maximum at 45° and its minimum along b. Here, e, defined as b/a, ranges from 0 to 1. And, θ varies from 0° and 180°, describes the orientation of the ellipse. The ellipse angle (ϵ), defined as $\epsilon = \tan^{-1}(e)$, varies from 0 to 45°, characterizing the shape of the E_{REP} (or E_{LEP}). E_{REP} and E_{LEP} are orthogonal in terms of handedness and θ, i.e., $E_{REP} \cdot E_{LEP}^\dagger = E_{REP}^\dagger \cdot E_{LEP} = a^2 - b^2 + ic(a - b) = 0$ under certain conditions. The schematic of the orthogonal EP used in this study is shown in Figure S1 (Supporting Information). The resultant polarization vector of the interference ($E_{LEP-REP}$) can be expressed as:

$$E_{LEP-REP} = \frac{1}{\sqrt{a^2 + b^2 + c^2}} \begin{bmatrix} (2a - ic) \cos \delta - c \sin \delta \\ ic \cos \delta + (2ib - c) \sin \delta \end{bmatrix} \tag{4}$$

Equation (4) describes how $E_{LEP-REP}$ generates spatial polarization modulation as a function of δ. Assuming the OEP forms purely polarization interference, we derived the spatial distribution of $E_{LEP-REP}$ with $e = 0.2, 0.3, 0.5,$ and 0.8, as shown in Figure 1. Further, let us denote the ellipticity of the interference beam (or interference ellipticity) by e_i and azimuth (or interference azimuth) by θ_i. Our results reveal that e_i and θ_i of the interference beam vary periodically. For OEP with $e = 0.2$, the interference polarization is linear for $\delta = 0\pi, \pi,$ and 2π, and EP otherwise. Furthermore, e_i and θ_i periodically vary depending on e of the writing beam. In particular, as e increases from 0.2 to 0.8, e_i decreases, suggesting that manipulating e can produce intriguing phenomena. Our analysis focuses solely on the spatial distribution of polarization, neglecting the amplitude modulation. We assume that all diffraction originates from surface relief. No separate birefringence contribution is taken into consideration.
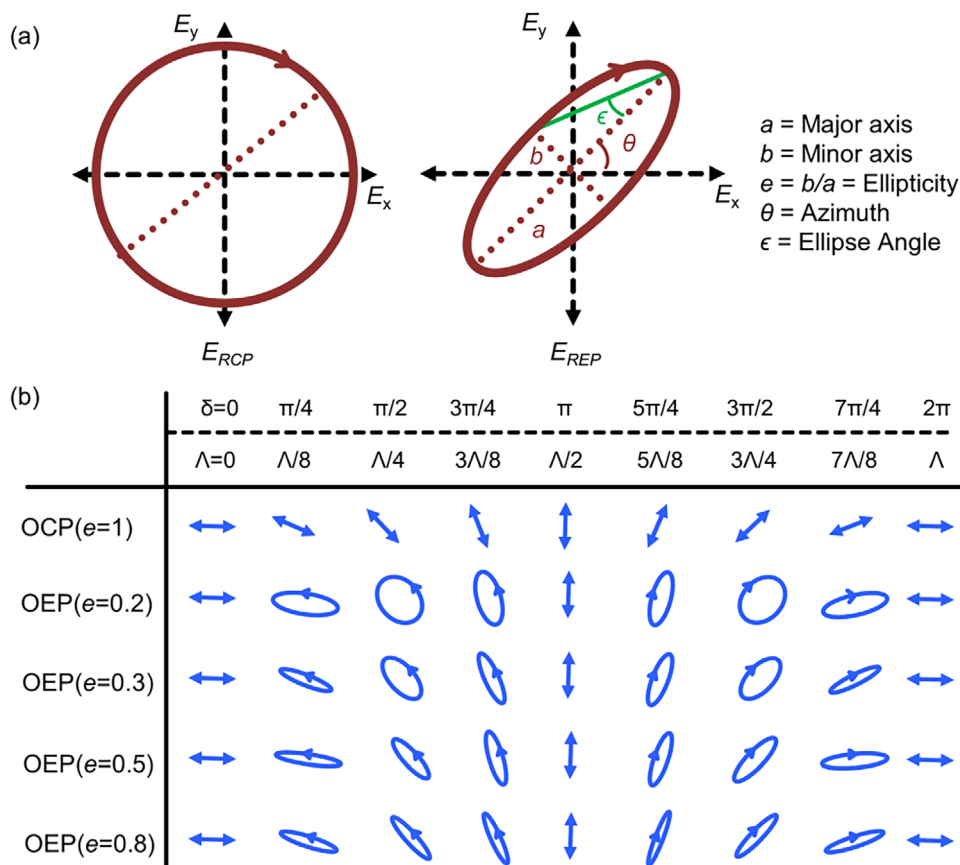
Figure 1. a) Schematic representation of E_{RCP} and E_{REP}. Here, ϵ and θ represents the ellipse angle and azimuth angle of EP, respectively. b) Spatial distribution of polarization states for OCP and OEP with e = 0.2, 0.3, 0.5, and 0.8.

3. Results and Discussion

3.1. Characterization of Azo Polymer

The absorption spectra of poly(disperse red 1 acrylate) known as PDR1A obtained from Merck exhibits a broad green absorption peak centered at 470 nm, as shown in **Figure 2a**. The utilized laser wavelength, 532 nm, falls within this absorption peak range. The molecular structure of PDR1A, as shown in the inset of Figure 2a, consists of photochromic azobenzene attached to the main chain polymer via the acrylate functional group. Upon absorption of 532 nm photons, the PDR1A molecules undergo a cyclic structural transition between *cis*- and *trans*-isomerizations states. These isomer's unique geometry leads to conformational changes in the range of 4 Å(Figure S2, Supporting Information). These conformational differences due to cyclic photoisomerization induce macroscopic mass migration of PDR1A, resulting in surface reliefs. This mass migration is dependent on photon energy and sensitive to polarization direction, meaning that the mass migration of azopolymer is influenced by both irradiation intensity and polarization direction. The underlying mechanism of such surface modulation formation can be found elsewhere.[5,32]

The experimental setup for the single-step HI is shown in Figure 2b. The linearly polarized green light is expanded, colli-

mated, and split into two orthogonal beams using PBS. These beams are then directed toward the sample to create an interference pattern. The polarization state is controlled by adjusting of P, QWP, and HWP. Specifically, by adjusting HWP1(HWP2) and QWP1(QWP2), OCP and OEP with desired ellipticity are produced, while HWP0 before the beamsplitter regulates intensity. The fast axis of QWP1 (and QWP2) is aligned at 45° to the P1 (and P2) to achieve RCP (and LCP), respectively. The HWP1 and HWP2 are not employed for OCP. For EP, the HWP1 and QWP1 are simultaneously adjusted to create elliptical polarization with specific ellipticity. The linear polarization from HWP1 passes through QWP1 at an angle other than 45°, and the desired ellipticity is achieved by further adjusting the angle of HWP1 relative to QWP1. Similarly, HWP2 and QWP2 are adjusted to produce another EP state. To ensure orthogonality between both EP beams, HWP1 and HWP2 and QWP1 and QWP2 are adjusted equally in opposite directions. The ellipticity and azimuth of the generated EP are further validated using a polarimeter.

The polarization state is determined by measuring the beam intensity while rotating an additional analyzer aligned behind the QWP. A detailed description of the experimental procedure can be found elsewhere.[42,43] Figure 2c illustrates that the resulting intensity in polar plots remains unchanged for all polarizer's angles, indicating both interference beams exhibit circularly polarization state. The handedness of the circularly polarized beam is
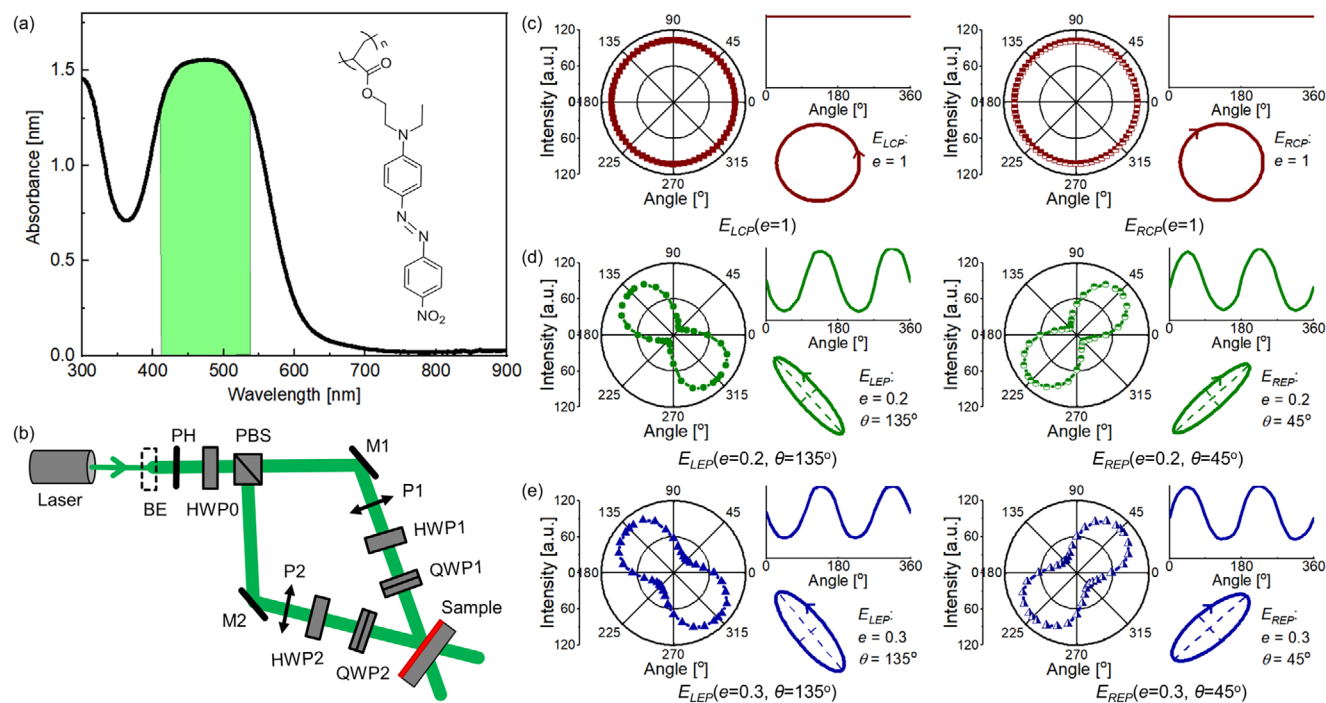
Figure 2. a) Absorption spectra of PDR1A and its molecular structure (inset). b) Schematic illustration of two-beam HI writing setup. BE: Beam Expander; PH: Pin hole spatial filter; PBS: Polarized Beam Splitter; HWP0, HWP1 and HWP2: Half-waveplates; M1 and M2: Mirrors; P1 and P2: Polarizers; QWP1 and QWP2: Quater-waveplates. The polarizer-angle dependent polar plots for estimating: c) OCP, d) OEP with $e = 0.2$, and e) OEP with $e = 0.3$. The normalized intensity variation as a function of the polarizer's angle is shown in each image. The schematic representation of obtained polarization is shown as the inset. The major and minor axes of EP are indicated as dotted lines in each case.

determined by the polarimeter and can also be inferred from the QWP angles. In the case of EP, e and θ are confirmed from the angle-dependent intensity measurements as shown in polar plots in Figure 2d. Clearly, the parameter b directly influences e. The handedness is estimated using the polarimeter and the angle of QWPs. In our experiments, both EP beams exhibit $e = 0.2$ and are orthogonal in terms of θ and handedness (Figure S3, Supporting Information). By adjusting the QWP1 and QWP2 away from $\pm 45°$ relative to HWP1 and HWP2, e can be increased further to 0.3, 0.5, and 0.8. The polar plots and normalized intensity curves confirm the achievement of OEP with $e = 0.3$, 0.5, and 0.8 (Figure 2e). After polarization measurements of writing beams, the additional polarizer is removed and proceeded with a single-step HI inscription on the azopolymer. Throughout the experiment, the interference angle remains fixed at 11°, and the inscription process takes about 20 min. For spatial multiplexing surface topography, the sample is rotated to a specific angle.

3.2. Ellipticity-Controlled Surface Topography

Following the essential characterizations of the prepared sample, we investigated the topography of 1D surface relief fabricated by OCP and OEP with varying ellipticity (e). We verified the PDR1A layer thickness influence on the surface modulation height of OCP grating and optimized the device fabrication (Figure S4, Supporting Information). The beam intensity was set to 100 mWcm^{-2}, and e was fixed at 0.2. An interference area of

~ 7 mm^2 was achieved on PDR1A (**Figure 3**). The direction of k_G is indicated as a white dotted arrow. The bright reflected light from the inscribed sample is due to the possible reflection of ambient light due to the visible wavelength range periodicity of surface topography. The obtained OM images of surface modulation are shown in Figure S5 (Supporting Information). The holograms of OCP (Figure 3a(i)) and OEP (Figure 3b(i)), along with OM images, reveal the creation of uniformly spaced surface reliefs. Additionally, the atomic force microscopy (AFM) images reveal sinusoidal topographies with a modulation height of 259 nm for OCP and 186 nm for the EP with $e = 0.2$. We achieved a constant pitch (Λ) of 715 nm with sinusoidal modulations. To further investigate the influence of ellipticity, the e of EP was increased to 0.3, 0.5, and 0.8, and performed interference inscription. As illustrated in Figure 3c–e, it's evident that the e has a substantial impact on surface modulation height. A slight reduction in modulation height to 146 nm was observed for $e = 0.3$, while $e = 0.5$ and 0.8 resulted in modulation heights of 120 and 160 nm, respectively. Notably, the topographical profile consistently maintained a sinusoidal form, exhibiting excellent agreement with the theoretical sinusoidal modulation predicted by scalar diffraction theory for two-beam interference: $h(x) = \frac{h}{2}[1 + sin(\frac{2\pi x}{\Lambda})]$, as shown in Figure S6a–e (Supporting Information). Since the interference angle remains unaltered, the Λ is invariant, resulting in a constant diffraction angle of 52°. Only first-order diffraction were observed on either side of the zeroth order, with the intensity equally distributed between them. As indicated in the Figure 3a–e(iv), the
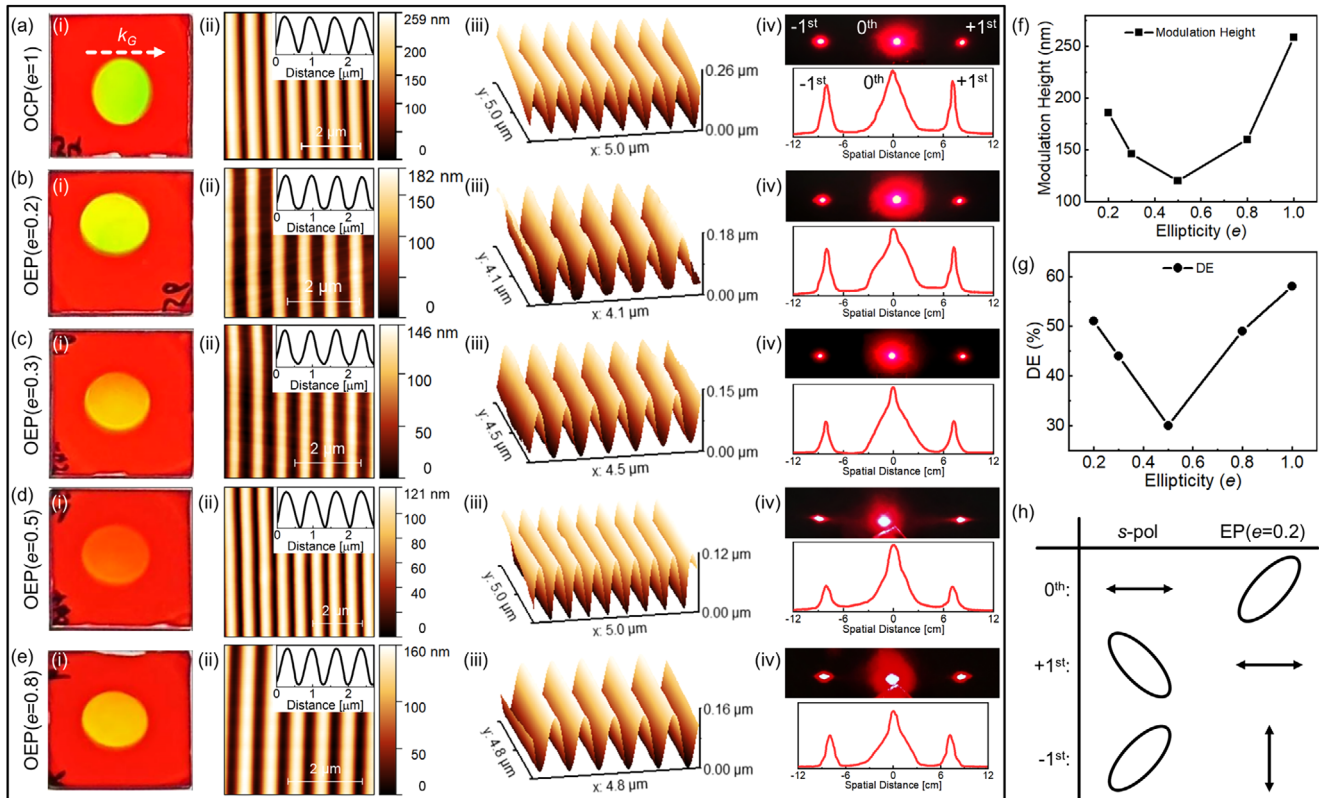
ADVANCED
SCIENCE NEWS

www.advancedsciencenews.com

LASER
&PHOTONICS
REVIEWS

www.lpr-journal.org

Figure 3. The characterization of ellipticity controlled 1D surface topography: a) LCP-RCP. b) OEP with $e = 0.2$, c) OEP with $e = 0.3$, d) OEP with $e = 0.5$, and e) OEP with $e = 0.8$. For each case: (i) Photographic images of the inscription, (ii) AFM images showing 2D topography with surface profile shown insert, (iii) AFM images showing 3D topography, and (iv) The obtained diffraction pattern and diffraction intensity distribution. Obtained surface modulation height (f) and DE (g) as a function of e. h) Schematic representation of polarization state of the diffracted beam from OEP($e = 0.2°$).

diffracted beam intensity distribution is also significantly affected by the writing beam ellipticity.

The obtained surface modulation height as a function of e is shown in Figure 3f. As e increases, the surface modulation height initially decreases up to $e = 0.5$ and then increases further. Interestingly, the e has a threshold value of 0.5 for modulation height. A similar trend is observed in the DE, as shown in the Figure 3g. The DE is defined as $\frac{I_{\pm 1}}{I_{tot}} \times 100$, where $I_{\pm 1}$ is the intensity of positive and negative first orders, and I_{tot} is the total incident intensity. The DE of OCP is 58% and OEP with $e = 0.2$, 0.3, 0.5, 0.8 are 51%, 44%, 30%, 49%, respectively. As e increases, DE decreases until $e = 0.5$, and then it increases again. This indicates that e has a threshold value of 0.5 for DE. Our results demonstrate that, as expected, surface modulation height and DE are intrinsically related to the first-order Bessel function associated with the maximum phase difference between sinusoidal reliefs, represented by: $\frac{2\pi(n_{poly}-1)\Delta h}{\Lambda}$, where n_{poly} is refractive index of polymer, where the phase difference is directly proportional to the modulation height.

Further, the polarization properties of the diffracted beam were examined for OEP($e = 0.2$) using a $s - pol$ and EP($e = 0.2, \theta = 45°$) read-out beams. We emphasize that the read-out EP($e = 0.2, \theta = 45°$) is the same as one of the writing beams. Notably, the polarization state of the zeroth-order diffracted beam remained s-polarized, the same as the read-out beam. However, the first-

order diffracted beam turns into elliptically polarized with an ellipticity (e_D) of 0.3 and orthogonal azimuth (θ_D) angle of $\pm 45°$, as illustrated in Figure 3h (polar plots shown in Figure S7a, Supporting Information). It should be noted that e_D and θ_D are ellipticity and the azimuth of the diffracted beam, respectively. The presented polar plots reveal we achieved 45° rotation of the polarization state in the first order by introducing a $\pi/8$ phase shift to the incident beam. A slight increase in e_D for the first diffraction order, when compared to the e was noticed, and we inferred to have no correlation with e. In another case, when EP($e = 0.2$) beam, identical to the writing beam, was used as a read-out beam, the diffracted beam becomes LP, as shown in Figure 3h (polar plots shown in Figure S7b, Supporting Information). In this case as well, a 45° rotation of the polarization state was achieved due to $\pi/8$ phase shift introduced to the incident polarization by the sample. Owing to the constant phaseshift, the present system demonstrates the ability to act as a wave plate with retardation other than a quarter-wave or half-wave plate.

If the orthogonally polarized beams are employed in HI, the spatial distribution of the polarization state as a function of δ ranging from 0 to 2π arises. For instance, OCP($e = 1$) produces spatially oriented LP varying in the plane of the sample with constant intensity. This creates a surface modulation comprised of continuous peaks and valleys, corresponding to LP lying perpendicular and parallel to the k_G, respectively, as depicted in **Figure 4**. Specifically, the peak occurs where the LP oriented 90° to the k_G
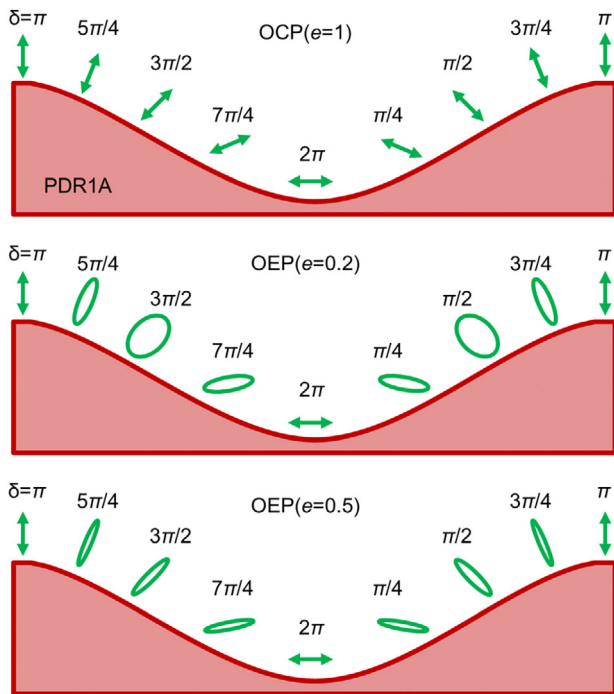
Figure 4. The schematic representation of the spatial distribution of polarization states as a function of δ for OCP, OEP($e = 0.2$), and OEP($e = 0.5$).

and the valley occurs at 0°. The region between the peak and valley, i.e., steep region, is LP continuously varying from 0° to 90°. However, in the case of OEP, while the polarization states corresponding to peaks and valleys remain LP, the space between them is no longer LP. For OEP, the EP with spatially varying e_i emerges for $\delta = \pi/4$ to $3\pi/4$ and $5\pi/4$ to $7\pi/4$. In particular, for OEP ($e = 0.2$), EP with spatially varying e_i and θ_i forms between $\delta = \pi/4$ to $3\pi/4$ and $5\pi/4$ to $7\pi/4$. In the case of OEP ($e = 0.3$), the interference beam exhibits EP with lower e_i between $\delta = \pi/4$ to $3\pi/4$ and $5\pi/4$ to $7\pi/4$. If e increases, e_i decreases, consequently h decreases. The relation between e_i and h suggests the photoisomerization effect in the steep regions also significantly affects the topography by either enhancing the peak's or slow-sown valley's photoisomerization effect. Another interesting point to emphasize is that the e has a threshold value of 0.5 for modulation height, even though the e_i and θ_i don't show this trend. However, notably, these spatial differences in e_i between peaks and valleys do not significantly impact the shape of the 1D topography, but they have a significant impact on modulation height and, consequently, on DE. These results indicate that even small alterations to the interference beams can significantly impact surface topography. Therefore, e_i offers an additional degree of freedom in controlling the final surface topography. These findings suggest that OEP is a viable approach for fabricating surface modulations.

3.3. EP Multiplexed Surface Topography

Next, we developed spatially multiplexed hierarchical patterns using the OEP beam with an e of 0.2. The light intensity was increased to 150 mWcm^2 while keeping the other parameters unchanged. The spatial multiplexing angles were set at 90° (double), 45° (triple), and 30° (quadruple) with respect to the first k_{G1}, as shown by white dotted lines on the sample in **Figure 5**. The k_{G1} refers to the grating axis of the first inscription. These hierarchical multiplexed surfaces prominently reflect ambient light.

For double-multiplexing, Figure 5a, both 2D and 3D surface profiles obtained by AFM show square-like pillars, contrasting with the sharp peaks in conventional multi-writing with orthogonal circular polarizations Figure S8 (Supporting Information). Specifically, the OCP produces an ideal sinusoidal modulation profile with a height of 308 nm, whereas the OEP produces a distorted sinusoidal profile with a matching pitch. The deviation from an ideal square shape for pillars is likely due to the spatially varying e_i. Each micropillar has a modulation height of 248 nm and a pitch of 853 nm, as shown in Figure 5a(iv). The OM image of double-multiplexing and the orientation of k_{G1} and k_{G2} is shown in Figure S9 (Supporting Information). We further evaluated our spatial multiplexed modulations through light diffraction observations using $s -$ polarized beam. As shown in Figure 5a(v), we achieved a 2D diffraction pattern with each diffraction order having a DE of 16%. The diffraction angles remain constant at 52° for all diffraction orders. From the evolution of the polarization state of the diffracted beam, we found that the polarization properties were similar to the 1D case. Specifically, for the $s -$ polarized readout beam, we achieved EP with e_D of 0.3 with orthogonal conjugate orders. In other words, the H_{+1} ($\theta_D = 45°$) and H_{-1} ($\theta_D = 135°$) are orthogonal terms of θ_D. Similarly, V_{+1} ($\theta_D = 60°$) is orthogonal to V_{-1} ($\theta_D = 100°$). A similar trend was observed in OCP. It reveals that the incident polarization state encountered a $\sim \pi/8$ phase shift to both perpendicular diffraction orders. Furthermore, the horizontal and vertical orders are perpendicular, confirming the associated geometry of perpendicular k_G's.

In the case of triple-multiplexing, we achieved discrete rhombus-like pillars with a height of 183 nm, shown in both 2D and 3D surface profiles, as shown in Figure 5b. By architecting three grating axes (k_{G1}, k_{G2}, and k_{G3}), we achieved the rhombus-like pillars. However, these structures exhibit a slight distortion from ideal rhombus geometry. This distortion arises from the asymmetric migration of azopolymers, driven by the spatially varying interference ellipticity e_i in the steep regions of the topography. The initial double multiplexed topography produces slightly distorted square-like pillars. The subsequent introduction of the k_{G3} through triple-multiplexing introduced further directional distortion, ultimately resulting in largely distorted rhombus shapes. Notably, the initial sinusoidal topography deformed with each multiplexing step, evolving from a sinusoidal pattern to discrete square-like pillars and finally to largely distorted rhombus-like micropillars, as shown in Figure 5b(iv). Consequently, a new diffraction order (1,−1) emerged with a DE of 10%, while maintaining the same diffraction angle (Figure 5b(v)). Although a slight decrease in DE was noticed due to differences in surface modulation height, the diffraction angles remained unchanged. Remarkably, the conjugative diffraction (−1,1) was negligible. This critical behavior is likely to originated from the structural distortion of rhombus-like pillars, which causes preferential light energy distribution into specific diffraction orders. Interestingly, the new diffraction order (1,−1) appeared close to
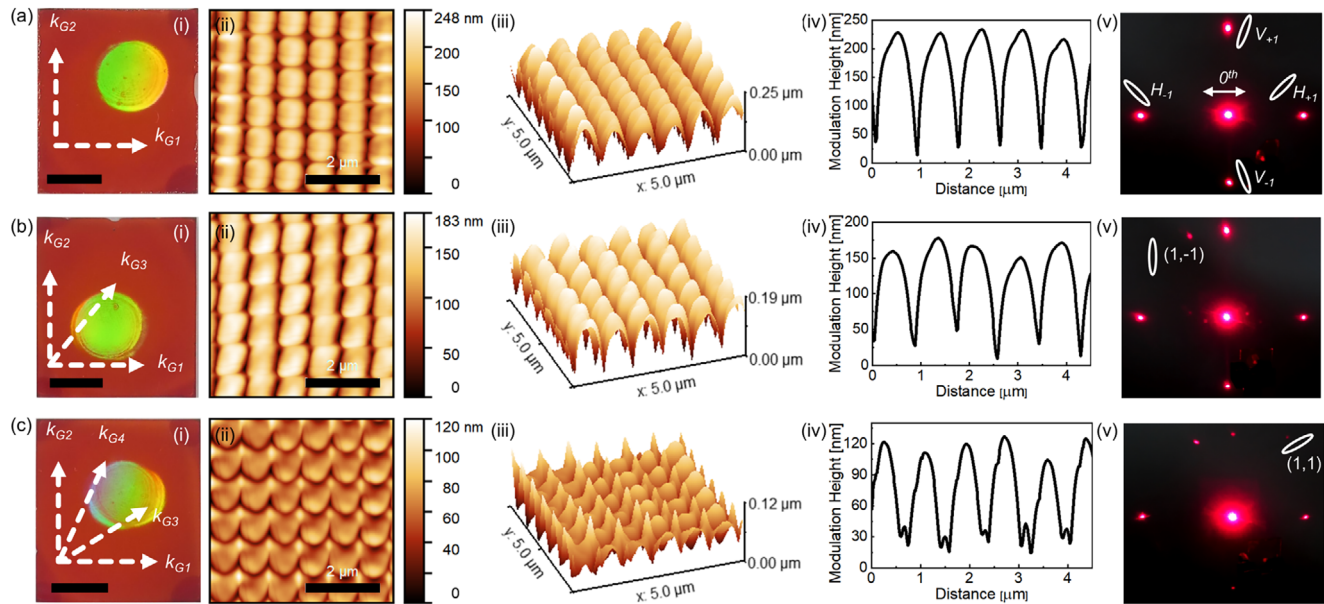
Figure 5. Multiplexed patterns by OEP with $e = 0.2$. a) Double inscription with 90°. b) Triple inscriptions, each with an angle of 45°. c) Quadruple inscriptions, each with an angle of 30°. a–c) (i) The spatially multiplexed sample with indicated k_G. The scale bar equals 5 mm. (ii) 2D surface topography. The scale bar is 2 μm (iii) 3D surface topography. (iv) Surface modulation height. (v) The diffraction pattern of the reconstructed beam and corresponding polarization states.

V_{+1}, despite the equally spaced multiplexed k_G's. This unusual control over the spatial frequency was achieved from the discrete distorted rhombus micropillar. However, e_D of diffraction order (1,–1) remained 0.3, while θ_D was found to be 90°.

To explore further capabilities of multiplexing, we increased the number of inscription steps to four (quadruple-multiplexing) and observed the resulting topological asymmetries and diffraction properties. As shown in Figure 5c (Figure S10, Supporting Information), the initial square micropillars formed in double-multiplexing gradually transformed into highly distorted shapes after quadruple-multiplexing. Since the double multiplexing of OCP shows ideal sinusoidal profiles in all 3D dimensions and the quadruple multiplexed OEP shows non-sinusoidal topographies, with controllable distortion created. Another noteworthy observation is that the modulation height decreases with each inscription. The initially formed 220 nm square pillars from the double-multiplexing are reduced to 120 nm non-symmetric micropillars in the fourth multiplexing, as shown in Figure 5c(iv). Both shape and size distortions are evident in this multiplexing. Furthermore, the increased distortion leads to the emergence of a pitch and more complex structural features. These findings suggest that while hierarchically multiplexed topography using OEP can provide the desired surface profile, the multiplexing steps are limited by accumulating distortions. As one can expect, a new diffraction order (1 1) is observed in the diffraction pattern with relatively low but significant DE, as shown in Figure 5c(v). Interestingly, again, this new diffraction order (1,1) appears close to the V_{+1} order. The k_G angles are proportional but similar to the triple multiplexed case, the diffraction angle remains unchanged, with only the lateral spatial frequency of diffraction order altered. This unusual nonsinusoidal modulation is merely achieved due to the non-uniform distribution of the azopolymer, caused by spatially varying e_i and θ_i between $\delta = \pi/4$ and $3\pi/4$. The polariza-

tion state of the (1,1) order remains EP with $e = 0.3$ and $\theta_D = 30°$. A $\pi/8$ phase shift is consistently introduced to all diffraction orders. Although the polarization state of the diffracted beam is unchanged from EP, the spatial modulation of θ_D is achieved. These results demonstrate that the spatially multiplexed HI inscription using OEP provides an additional degree of freedom in designing surface topography and achieving spatial control over the diffracted beam. However, during higher multiplexing, careful consideration must be given to the selection of e and angles of k_G, and lateral intersection angles of topographies.

The reported unconventional approach of utilizing ellipticity-controlled OEP in HI technique holds great potential for fabricating multiplexed 2D and 3D surface topographies. While the ellipticity of OEP may not greatly impact 1D surface modulation, it has a substantial influence on spatial multiplexing. However, a higher level of multiplexing can distort the topography. In contrast, multiplexing with OCP is well-known for producing quasicrystalline topographies, as demonstrated elsewhere.[15,32,44] Notably, the major difference between OCP and OEP, as shown by the spatial distribution of polarization states depicted in Figure 1, lies in the spatial variation of e_i and θ_i between $\delta = 0$ to π and π to 2π, i.e., between the peaks and the valley corresponds to steep region. From this observation, we deduce that e_i and θ_i in the steep region tend to modulate topography due to the asymmetric lateral distribution of azopolymer. This implies that polarization ellipticity, beyond influencing the peaks and valleys of topography, also significantly affects topography and subsequent diffraction properties. The local distribution of the polarization and ellipticity of the interference beam provides an additional degree of freedom for controlling surface topography. By carefully selecting the ellipticity of the interference beam, one can achieve greater control over structural features. These unique distorted features enable control over the diffracted light and polarization

that opens possibilities for advanced optical elements with customized properties. This approach simplifies the fabrication of complex optical components like OFE and PCs for a variety of applications.

4. Conclusion

This study presents an unconventional approach to fabricating optical elements comprised of 3D structural features using ellipticity-controlled OEP in the HI technique. By manipulating the ellipticity of OEP through spatial multiplexing, we achieved surface topographies consisting of distorted square-like pillars arising from the asymmetric lateral migration of azopolymer molecules, enabling asymmetric spatial control of diffracted light. Increasing the number of multiplexing further enhances this distortion, subsequently shifting square-like shapes toward rhombus-like pillars. This shape transformation provides further control over both the structural features and the diffraction properties, such as DE and spatial frequencies. This approach facilitates the asymmetric migration of azopolymer due to the spatially varying ellipticity and azimuth of the polarization state between topographical peaks and valleys, providing additional control over the diffracted beam. Further, we aimed to establish a clear relationship between the parameters e, e_i, and e_D, and the resulting $\pi/8$ phase shift effectively converts LP incident light to EP. By considering the limitations imposed by the number of spatial multiplexing, the device optimization was done on the layer thickness, e, e_i, and device topography. Further studies are necessary to overcome these limitations. Overall, ellipticity-controlled EP could be a potential alternative to OCP, offering easier production and an additional degree of freedom, thereby enabling the fabrication of complex optical elements such as PC and OFE.

5. Experimental Section

Materials: The ellipticity-controlled multiplexed surface relief was fabricated by dispersing 8 wt% amorphous azopolymer PDR1A (From Merck) into 1,1,2-trichloroethane (From Merck) solvent. To improve the solubility of PDR1A into the solvent, the mixture was mechanically mixed for 30 min and subsequently heated to 60°C for 1 h. The sample was then filtered through a 1 µm PTFE syringe filter to remove any undissolved PDR1A particles. Finally, the obtained homogeneous mixture was spin-coated onto a cleaned substrate at room temperature. The time gap between spin coating and interference writing is adjusted to ∼ 1 h.

Methods: The absorption spectra of PDR1A were measured using a UV–visible spectroscope (Jasco, V-760). The ellipticity-controlled multiplexed surface topography on the amorphous azopolymer PDR1A film was achieved using a single-step two-beam HI technique. The PIP interference was generated by a single-frequency diode laser emitting at a 532 nm green wavelength (Cobolt, Hubner Photonics). Surface topography was examined using a polarized optical microscope (POM) (Nikon, Eclipse LV100POL) with a single polarizer and AFM (HITACHI, AFM5000) in non-contact cantilever mode. Diffraction properties were observed using a 632.8 nm He-Ne laser (HNL020LB, Thorlabs) with an intensity of 7.6 mWcm^{-2} and s-polarization and EP ($e = 0.2$). The polarization axis of the readout beam is always parallel to the k_G (or k_{G1}). The readout beam does not disrupt the surface modulation as it falls out of the absorption peak of PDR1A shown in Figure 1a. Diffraction patterns were captured under far-field diffraction conditions (Fraunhofer diffraction) by placing the screen 5.2 cm behind the sample and capturing images with a digital camera. The handedness of the signal beam, readout bean, and diffracted beam

was also estimated using both the Polarizer rotation method and the Polarimeter (PAX1000VIS, Thorlabs).

Conflict of Interest

The authors declare no conflict of interest.

Data Availability Statement

The data that support the findings of this study are available from the corresponding author upon reasonable request.

[1] Z. Lv, J. Liu, L. Xu, *IEEE Photonics J.* **2021**, *13*, 1.
[2] H.-J. Yeom, H.-J. Kim, S.-B. Kim, H. Zhang, B. Li, Y.-M. Ji, S.-H. Kim, J.-H. Park, *Opt. Express* **2015**, *23*, 32025.
[3] Y. Li, Q. Yang, J. Xiong, K. Yin, S.-T. Wu, *Opt. Express* **2021**, *29*, 42696.
[4] M. Salvatore, F. Borbone, S. L. Oscurato, *Adv. Mater. Interfaces* **2020**, *7*, 1902118.
[5] Y. Lim, B. Kang, S. Lee, *Adv. Funct. Mater.* **2021**, *31*, 2100839.
[6] J. Jelken, C. Henkel, S. Santer, *Appl. Phys. B* **2020**, *126*, 1.
[7] S. L. Oscurato, F. Reda, M. Salvatore, F. Borbone, P. Maddalena, A. Ambrosio, *Adv. Mater. Interfaces* **2021**, *8*, 2101375.
[8] J. Vapaavuori, R. H. Ras, M. Kaivola, C. G. Bazuin, A. Priimagi, *J. Mater. Chem. C* **2015**, *3*, 11011.
[9] N. K. Viswanathan, D. Y. Kim, S. Bian, J. Williams, W. Liu, L. Li, L. Samuelson, J. Kumar, S. K. Tripathy, *J. Mater. Chem.* **1999**, *9*, 1941.
[10] F. Reda, M. Salvatore, F. Borbone, P. Maddalena, S. L. Oscurato, *ACS Mater. Lett.* **2022**, *4*, 953.
[11] F. Yang, Y. Murakami, M. Yamaguchi, *Optical Review* **2013**, *20*, 13.
[12] N. Lassaline, R. Brechbühler, S. J. Vonk, K. Ridderbeek, M. Spieser, S. Bisig, B. Le Feber, F. T. Rabouw, D. J. Norris, *Nature* **2020**, *582*, 506.
[13] S. L. Oscurato, F. Reda, M. Salvatore, F. Borbone, P. Maddalena, A. Ambrosio, *Laser Photon. Rev.* **2022**, *16*, 2100514.
[14] Y. Lim, B. Kang, S. J. Hong, H. Son, E. Im, J. Bang, S. Lee, *Adv. Funct. Mater.* **2021**, *31*, 2104105.
[15] M. Guo, Z. Xu, X. Wang, *Langmuir* **2008**, *24*, 2740.
[16] J. Choi, W. Cho, Y. S. Jung, H. S. Kang, H.-T. Kim, *ACS nano* **2017**, *11*, 1320.

[17] J. Kumar, L. Li, X. L. Jiang, D.-Y. Kim, T. S. Lee, S. Tripathy, *Appl. Phys. Lett.* **1998**, *72*, 2096.

[18] T. Todorov, L. Nikolova, N. Tomova, *Appl. Opt.* **1984**, *23*, 4588.

[19] T. G. Pedersen, P. M. Johansen, N. C. R. Holme, P. Ramanujam, S. Hvilsted, *Phys. Rev. Lett.* **1998**, *80*, 89.

[20] B. Bellini, J. Ackermann, H. Klein, C. Grave, P. Dumas, V. Safarov, *J. Phys.: Condens. Matter* **2006**, *18*, S1817.

[21] N. K. Viswanathan, S. Balasubramanian, L. Li, J. Kumar, S. K. Tripathy, *J. Phys. Chem. B* **1998**, *102*, 6064.

[22] C. J. Barrett, P. L. Rochon, A. L. Natansohn, *J. Chem. Phys.* **1998**, *109*, 1505.

[23] C. J. Barrett, A. L. Natansohn, P. L. Rochon, *J. Phys. Chem.* **1996**, *100*, 8836.

[24] P. Pagliusi, B. Audia, C. Provenzano, M. Pinol, L. Oriol, G. Cipparrone, *ACS Appl. Mater. Interf.* **2019**, *11*, 34471.

[25] L. W. Giles, C. F. Faul, R. F. Tabor, *Mater. Adv.* **2021**, *2*, 4152.

[26] H. Audorff, R. Walker, L. Kador, H.-W. Schmidt, *J. Phys. Chem. B* **2009**, *113*, 3379.

[27] J. Strobelt, D. Stolz, M. Leven, M. Van Soelen, L. Kurlandski, H. Abourahma, D. J. McGee, *Opt. Express* **2022**, *30*, 7308.

[28] F. Reda, M. Salvatore, F. Borbone, P. Maddalena, A. Ambrosio, S. L. Oscurato, *Opt. Express* **2022**, *30*, 12695.

[29] S. L. Oscurato, M. Salvatore, P. Maddalena, A. Ambrosio, *Nanophotonics* **2018**, *7*, 1387.

[30] S. Moon, C.-K. Lee, S.-W. Nam, C. Jang, G.-Y. Lee, W. Seo, G. Sung, H.-S. Lee, B. Lee, *Sci. Rep.* **2019**, *9*, 6616.

[31] J. Jo, D. Baek, H. Hugonnet, K. Kim, H. Ji, Y. Lim, T. Kim, S. Lee, Y. Park, *Adv. Opt. Mater.* **2024**, *12*, 2302048.

[32] K. Kim, Y. Lim, H. Son, S. J. Hong, C.-W. Shin, D. Baek, H. H. Kim, N. Kim, J. Bang, S. Lee, *Adv. Opt. Mater.* **2022**, *10*, 2201421.

[33] Z. Huang, C. Wu, Y. Chen, X. Lin, X. Tan, *Opt. Express* **2020**, *28*, 23679.

[34] T. Sasaki, E. Nishioka, K. Noda, M. Kondo, N. Kawatsuki, H. Ono, *Jpn. J. Appl. Phys.* **2014**, *53*, 02BB06.

[35] H. Ono, M. Nakamura, A. Emoto, N. Kawatsuki, *Jpn. J. Appl. Phys.* **2010**, *49*, 032502.

[36] Z. Huang, Y. He, T. Dai, L. Zhu, Y. Liu, X. Tan, *Optical Engineering* **2020**, *59*, 102409.

[37] L. Shao, J. Zang, F. Fan, Y. Liu, X. Tan, *Appl. Opt.* **2019**, *58*, 9983.

[38] Y. Zhang, G. Kang, J. Zang, J. Wang, Y. Liu, X. Tan, T. Shimura, K. Kuroda, *Optics Letters* **2016**, *41*, 4126.

[39] Z. Huang, Y. He, T. Dai, L. Zhu, X. Tan, *Opt. Las. Eng.* **2020**, *131*, 106144.

[40] R. Azzam, N. Bashara, *Ellipsom. Polariz. Light*, North-Holland personal library, North-Holland, **1987**.

[41] F. Pedrotti, L. Pedrotti, *Introduct. Optics*, Prentice Hall, **1993**.

[42] R. Manda, S. Pagidi, Y. J. Heo, Y. J. Lim, M. S. Kim, S. H. Lee, *Adv. Mater. Interfaces* **2020**, *7*, 1901923.

[43] R. Manda, S. Pagidi, S. S. Bhattacharya, H. Yoo, A. Kumar, Y. J. Lim, S. H. Lee, *J. Phys. D: Appl. Phys* **2018**, *51*, 185103.

[44] K.-H. Kim, Y.-C. Jeong, *Opt. Express* **2018**, *26*, 5711.